Full-waveform inversion as a tool to predict fault zone properties

Ahmed M. Alghuraybi[1*], Rebecca E. Bell[1], Christopher A.-L. Jackson[1], Melissa Sim[1], Shuhan Jin[1]

[1] *Landscapes and Basins Research Group (LBRG), Department of Earth Science and Engineering, Imperial College London, UK.*

ORCID ID: FA, 0000-0003-0584-8687; SA, 0000-0002-4785-9707; TA, 0000-0002-8592-9032

*Corresponding author (e-mail: a.alghuraybi19@imperial.ac.uk)

Abstract

Understanding the physical properties of fault zones is essential for various subsurface applications, including carbon capture and geologic storage, geothermal energy, and seismic hazard assessment. Despite improvements in fault imaging and visualisation, predicting the physical properties of faults and fault zones in the subsurface remains challenging, even with high-quality seismic reflection data. In this study, we use borehole and high-quality Post-Stack Depth Migrated (PSDM) seismic reflection and Full-Waveform Inversion (FWI) velocity data to investigate the characteristics of fault zones in the Samson Dome in the SW Barents Sea. We analyse the variance attribute of the PSDM and FWI volumes, revealing linear features that consistently appear in both datasets. These features correspond to locations of rapid velocity changes and seismic trace distortions, which we interpret as faults. These observations demonstrate the capability of FWI in recovering fault zone velocity structures. Our findings also reveal the natural heterogeneity and complexity of fault zones, with varying P-wave velocity anomalies within the studied fault network. We propose that these anomalies may indicate differences in fault transmissibility. Our study highlights the potential of FWI velocity models in predicting fault zone physical properties and improving subsurface interpretations. By integrating seismic reflection data and FWI models, we can enhance our understanding of fault zone architecture, which has implications for energy transition policies, carbon storage, geothermal energy development, waste disposal, and seismic hazard mitigation.

Supplementary material: Additional seismic depth slices are available at https://doi.org/xxxx.

Faults play a major role in controlling subsurface fluid flow by juxtaposing impermeable lithologies against permeable ones, or by containing fine-grained, low-permeability (i.e., sealing) fault rocks (e.g., Welbon et al., 1997; Bailey et al., 2006). Determining the sealing potential of faults typically involves the integration of seismic reflection and wellbore data (e.g., Manzocchi et al., 2010; Yielding et al., 2010). Historically, understanding the variability in fault permeability played a major role in hydrocarbon exploration, production and in determining compartmentalisation, and overall economic viability of hydrocarbon reservoirs (e.g., Bailey et al., 2002; Jolley et al., 2010; Fisher et al., 2018). However, a better understanding of the subsurface and more specifically the hydraulic properties of faults, is increasingly required to comply with government-mandated regulations and to provide public assurances of several net-zero solutions (e.g., Kaldi et al., 2013), whether this relates to carbon capture and geologic storage, producing geothermal energy, designing radioactive waste disposal sites, locating water resources, or mitigating seismic hazards (e.g., de Laguna et al., 1968; Morris et al., 2004; Chiaramonte et al., 2015; Morell et al., 2018; Daniilidis et al., 2021; BGS, 2022).

Seismic reflection data have been widely used to reveal the presence, geometry, and evolution of subsurface structures, including normal faults (e.g., Boyer & Elliott, 1982; Childs et al., 2003). Traditionally, those studies involve seismic interpretation workflows to map discontinuities in seismic sections that delineate offsets in stratal reflections (e.g., Wernicke, 1995). Although often expressed as discrete, planar features, field data show that faults comprise zones of deformation (e.g., Kim et al., 2004; Childs et al., 2009). Previous studies using seismic reflection data have demonstrated that normal faults are expressed as seismic disturbance zones (*sensu* Iacopini et al., 2016). The extent of the related fault damage zone can be visualised using seismic attributes, and it has been shown to be of comparable width to exposed damage zones (e.g., Alaei & Torabi, 2017). The way a fault is expressed in seismic reflection data depends on the frequency and quality of the seismic data, with faults appearing as planar features at low frequencies and as zones or extractable bodies or volumes at higher frequencies (e.g., Botter et al., 2016).

It has been long recognised that mapping faults using seismic reflection data is a relatively subjective exercise, especially in terms of defining fault geometries in map-view and the displacement distribution across a faults surface (e.g., Freeman et al., 1990). This appreciation of subjectivity caused several authors to focus more on finding robust and perhaps more objective interpretation methodologies that utilise the full extent of the imaging power of seismic reflection data (e.g., Freeman et al., 1990; Hesthammer et al., 2001; Braathen et al., 2009). For example, seismic attributes have been developed to identify faults and permit more detailed analysis of their geometries (e.g., Jones & Knipe, 1996; Randen

et al., 2001; Chopra & Marfurt, 2005; Iacopini & Butler, 2011) and the style and magnitude of related (i.e., offset) strain (e.g., Freeman et al., 2008; Braathen et al., 2009; Iacopini et al., 2016). More recently, machine learning and increased computational power have allowed the development of data-driven, automated fault interpretation workflows (e.g., Meldahl et al., 2001; An et al., 2021; Wrona et al., 2021; An et al., 2023). However, despite these improvements in fault imaging and visualisation, predicting the physical properties of faults and fault zones (i.e., fault zone width, shale/clay smear content, transmissibility, and fluid content) in the subsurface remains challenging, even with high-quality seismic reflection data.

Full-waveform inversion (FWI) is an advanced method of seismic imaging that aims to recover high-fidelity physical property models of the subsurface using the full recorded wavefield (i.e., both reflection and refraction waves) from seismic surveys, as opposed to traditional velocity modelling workflows based on first-arrivals (e.g., Virieux & Operto, 2009; Morgan et al., 2013; Warner et al., 2013 for more details). Theoretically, any physical properties of rock units that influence seismic waves (such as P-wave, S-wave velocities, and density) can influence the recorded seismic wavefield and, therefore, be revealed by FWI models (e.g., Warner et al., 2013; Tromp, 2020; Davy et al., 2021). However, in practice, the majority of FWI studies, particularly in 3D, have focused on the recovery of P-wave velocity. Some of these FWI studies in subduction zones and sedimentary basins have qualitatively demonstrated the ability of FWI models to image fault zones characterised by varying velocities relative to their surrounding host rocks (e.g., Morgan et al., 2013; Gray et al., 2019; Davy et al., 2021). We hypothesise that this velocity variability is related to changes in fault zone hydraulic properties, as captured by parameters such as Shale Gouge Ratio (SGR). As such, the FWI itself may be a potential 'screening' tool to assess fault transmissibility within a fault network. In this study, we test this hypothesis by using high-quality, depth-migrated 3D seismic reflection and FWI data from the Samson Dome, SW Barents Sea, offshore Norway. We compare our recovered fault velocities with modern stress-field orientations and the results of tradition shale-gauge ratio methods (the current state-of-the-art in determining fault transmissibility; e.g., Bretan, 2023). Ultimately, we showcase initial attempts to improve our understanding of the physical properties of fault zones by combining seismic reflection and FWI velocity data.

Geological Setting

The Barents Sea is a shallow continental shelf that encapsulates an area of c. 1.3 million km2 offshore Norway between the Arctic Ocean to the north and the Russian and Norwegian coastlines to the south (e.g., Gabrielsen, 1984; Doré, 1995). The large-scale structures in the region were formed as a result of multiple phases of rifting from the Devonian to the opening of the Norwegian and Greenland seas and the onset of seafloor spreading in the Eocene (Faleide et al., 1984, 1993, 2008; Gabrielsen, 1984; Gabrielsen et al., 2016). Our study area is located over the Samson Dome, a structure thought to have formed due to salt movement during the Middle to Late Triassic (e.g., Breivik et al., 1994; Mattos et al., 2016). The stratigraphy in the Samson Dome is dominated by siliciclastic rocks, with minor carbonate intervals, particularly in the Lower Permian (e.g., Breivik et al., 1994). A detailed lithology report for wellbore 7224/7-1 can be found on the Norwegian Petroleum Directorate (NPD) webpage (https://factpages.npd.no/en/wellbore/PageView/Exploration/All/1245). A major unconformity likely formed in the Late Cretaceous to Paleogene, eroding part of the Upper Cretaceous capping the Samson Dome (e.g., Faleide et al., 2008). The sediments overlying the unconformity are associated with high seismic reflection amplitudes that are potentially caused by shallow gas (e.g., Jones et al., 2013).

Data

We used the BG1002R13 seismic reflection survey acquired by CGG and processed by BG Geophysical Operations in 2013. The data can be retrieved from the DISKOS database (https://portal.diskos.cgg.com/whereoil-data/). The survey is a 3D Narrow Azimuth (NAZ) seismic reflection survey acquired using a dual marine airgun source with 10 six-kilometre-long streamers and 480 receiver groups, defining a full-fold area of c. 1100 km^2. The group and flip-flop shot intervals were set to 12.5 m, whereas the spacing between cables was 100 m. A high-cut frequency filter of 200 Hz was applied along with a bandpass filter of 2-7 Hz. Additional filters and pre-processing steps applied to the raw data include swell noise attenuation and linear random de-noise with top and bottom mutes. The total recording length and initial sampling intervals are 5050 ms and 2 ms, respectively (Jones et al., 2013).

Various approaches were used to generate a good starting velocity model for the FWI, including a 1-D wellbore-derived blocky model, first arrival refraction tomography-based model and a constrained Dix inversion model of the stretched-to-depth pre-stack-time-migration root-mean-square velocity field (Jones et al., 2013). The FWI velocity model is then used to generate the final full-stack depth volume that runs from 0 m to 6000 m sampled every 10 metres. The data was processed using a zero-phase wavelet and displayed in reverse SEG polarity convention, i.e., a downward increase in acoustic impedance is

represented by a trough (coloured blue) and a decrease by a peak (coloured red). The seismic resolution is 10- 70 m.

In this study, we also used data from wellbore 7224/7-1, which was drilled in 1988 to evaluate the hydrocarbon reservoir potential of the Lower Jurassic and Upper Triassic sandstones and to improve previous structural and geophysical interpretations to better the understanding of the area (NPD, 2023). The wellbore drilled a total depth of 3067 m and provides age and lithological constraints down to the Lower Triassic (Olenekian). The age and lithological constraints allowed us to understand the character of the seismic reflection data and FWI expression of the faults.

Method

Our results are derived from two main approaches: 1) seismic interpretation, and 2) statistical analysis of seismically imaged fault properties, which we later consider in the context of the present regional stress field and calculated SGR. First, we mapped horizons and faults and generated seismic attributes using Petrel seismic interpretation software. In total, we mapped 15 horizons (11 tie to age-constrained formation tops proven by wellbore 7724/7-1, one marks the top of the acoustic basement, and three define regionally mappable intra-formational horizons; Fig. 1a). Our horizon mapping approach involved a coarse, first-pass interpretation with an in-line and x-line spacing of 100 x 250 (i.e., 1250 m x 3125 m). In areas where the seismic quality was poor or the reflections less-prominent and continuous, we mapped the horizons every 32 and 50 in-lines and x-lines, respectively (i.e., 400 m x 625 m). After this initial systematic mapping, we used 3D auto-tracking to populate the interpretation across the study area to fill gaps in our grid. We then manually interpreted (at 12.5 m spacing) reflections into areas where auto-tracking was not possible because they were discontinuous and characterised by low amplitude. In terms of fault mapping, we generated a variance seismic attribute to highlight signal discontinuities in the seismic reflection data (e.g., Randen et al., 2001). We computed the variance attribute for key depth slices and along key horizons. The variance attribute helped reveal the fault network and aided fault mapping. We also compared the variance attribute generated from the depth volume (PSDM) with variance time slices computed from the time volume (PSTM); this helped ensure the fault network geometry was consistently imaged and not unduly influenced by processing or depth conversion steps. Overall, we mapped 48 faults by combining the variance data and seismic cross-sections taken perpendicular to the local strike of each fault.

Following the seismic interpretation stage, we examined the FWI velocity volume to note any lateral velocity changes that could relate to faults. To do this, we first compare FWI velocity in-line and x-

line sections with corresponding seismic reflection depth surfaces (Fig. 2). This step revealed the expected general velocity increase with depth, but also shows some lateral changes in velocity along horizons and other linear features that correlate with faults interpreted in the seismic reflection data. We then extracted FWI velocity values along key horizons mapped in the PSDM volume (Figs. 3a, 4a). The two velocity surfaces showed clearly defined linear features with different velocities compared to the surrounding areas. These features align with mapped faults, which are observed in variance slices taken along H3 and H7, extracted from both the FWI velocity and PSDM volumes (Figs. 3, 4). While the application of the variance attribute on seismic reflection data (PSDM volume) detects edges or signal discontinuities that are often correlated to faults (e.g., Randen et al., 2001), computing the variance of the FWI volume highlights sudden changes in velocity. The application of the variance to FWI models is a novel approach that has not been reported previously as far as we are aware and, in this study, we attempted to test the reliability and performance of the variance on FWI models.

After visually confirming the correlation between the linear features in the FWI velocity volume and the fault network mapped in the PSDM volume, we then extracted the velocity values from the FWI model along each horizon as spatially positioned point data (i.e., XY coordinates with corresponding velocity data), thus allowing us to quantify any potential relationship. We also extracted velocity data along individual fault traces. This resulted in individual velocity datasets for each mapped fault and for each horizon. Given the fault trace geometries from the previous step, we could then extract the velocities for a defined fault zone width (i.e., fault damage zone; *sensu* Kim et al., 2004; Childs et al., 2009) and compare them to velocities at a set distance around the fault zone (i.e., to capture the velocity of unfaulted host-rock). In this study, we determined fault zone width from our mapped fault planes (i.e., the fault polygon width determined from our mapping of footwall and hangingwall cut-offs) and host rock width of 200 m taken around the fault zone polygon (Fig. 5). To compare the velocities between the two, we calculated and compared a moving average value for each. We also used representative strike-perpendicular profiles to detect any changes in velocity across fault zones, given the lack of obvious methods of determining the width of a fault zone using seismic reflection data and to account for any uncertainty in our defined fault zones (see Fig. 7.g as an example).

Lastly, we generated a combined attribute by computing a dip-steered, discontinuity-enhancing attribute from the FWI velocity volume and multiplying it by a PSDM variance volume. The newly generated combined attribute helps in 1) highlighting the faults and 2) detecting whether the fault zone velocity is higher (+) or lower (-) than the surrounding host rock velocity. We then compared the results

of our velocity analysis with regional present-day stress orientation and Shale Gauge Ratio (SGR) results (Alghuraybi et al., 2023), which provide insights into fault sealing potential. A summary of the workflow we used here is shown in Fig. 6.

Results

We studied a total of 48 faults and focused our analysis on the interval between H3 and H7 (Lower Jurassic to Upper Cretaceous) (Fig. 1a). This is because most faults tip out upwards into Lower Cretaceous strata and the resolution of the FWI velocity volume (as expected given the narrow-azimuth nature of these data) drastically decreases below 1.5 km (Appendix 1). The upper 1.5 km portion of the FWI model resolves linear features that are consistent with apparent faults on the corresponding PSDM seismic sections (Fig. 2). These linear features appear to locally have higher or lower P-wave velocities, whereas in other locations they appear to simply offset two blocks of different velocities (Fig. 2b).

By extracting the velocities on H3 and H7, we can see the general velocity trend in the area at each structural level (Figs. 3a, 4a). Overall, we observe a general velocity decrease towards the centre of the surface (i.e., towards the Samson Dome, where horizons generally become shallower; Figs. 3a, 4a). The velocity decrease towards the Samson Dome is logical as shallower horizons are expected to have slower velocities. This general observation provides confidence that the FWI velocity model is showing useful information about rock properties. However, we can also detect faults dissecting the dome; these are clearly defined by velocity characteristics that differ to their flanking host rock (Figs. 3a, 4a). The geometry of the faults seen in the FWI velocity surfaces is consistent with that observed in the PSDM variance surface (Figs. 3c, 4c). We also note that a variance attribute taken from the FWI velocity volume detects some of the faults seen on the PSDM variance (Figs. 3b, 4b). Although this qualitative velocity difference is apparent visually, one might argue that these differences are rather subtle and largely dependent on the dynamic range of the colour scale used to display the FWI velocity surface. However, the variance results demonstrate the ability of the FWI model to recover fault zones, as the same fault patterns are extracted from two largely independent datasets (PSDM- produced solely from reflections and FWI- driven largely by refracted arrivals). To supplement the variance analysis results, we next present a detailed quantitative analysis of three selected faults from the studied fault network. We selected these faults based on their strike, location relative to the dome, and kinematic history. These results are later compared to regional stress data and traditional fault seal analysis (i.e., SGR).

Fault 23 (F23) strikes NW-SE and is c. 6 km long (Fig. 7). F23 has a clear fault expression on the PSDM variance surfaces (Fig. 7b) and appears as a continuous zone of relatively low velocity on both FWI

velocity surfaces (Fig. 7c). Our combined fault zone velocity attribute shows F23 as a laterally continuous band of blue colour (i.e., lower fault zone velocity; Fig. 7d). The cross-plot of FWI velocities in and around F23 shows general agreement with the combined attribute results (Fig. 7d, e). However, our statistical analysis of the velocities reveals greater along-strike heterogeneity, with local zones of relatively high velocity occurring within the fault zone (Fig. 7f). For example, the SW end of F23 at the structural level of H3 shows a higher velocity as indicated by the positive difference between fault zone and host rock velocities (Fig. 7f.1). Similarly, at the structural level of H7, F23 appears to have a higher velocity towards its north-western end, and generally shows more fluctuation or scatter in the velocity difference between fault zone and host rock velocities at this structural level (Fig. 7f.2). These statistical differences can be confirmed by closely examining the FWI velocity surfaces (Fig. 7c), where minor velocity changes along-strike can be detected. Equally, variable velocity difference between fault zone and host rock velocities observed in the velocity analysis of F23 might be attributed to the fact that the fault is at the edge of the survey where the FWI model (and the PSDM) is more poorly constrained (Fig. 3c). These along-strike velocity variations might be interpreted as a result of noise or data artefacts. However, we observe similar velocity variations along faults which are not at the edge of the survey (Fig. 4.a). Therefore, it is more likely that these variations in velocity along-strike of the fault are recoding a physical response that reflects along-strike variations in fault displacement, fault zone width, and/or shale/clay smear content.

Unlike F23, Fault 30 (F30) is in the centre and is thus fully imaged within the dataset (Fig. 3c). F30 strikes ENE-WSE and is on top of the dome (Fig. 8). Even though we can see the expression of F30 on the PSDM variance surfaces, we also note the complex and more highly discontinuous nature of the PSDM variance surface at this location (Fig. 8b). This is likely a result of the highly faulted nature of the dome crest, which can be seen by the PSDM variance slice in Fig. 3c. In terms of FWI velocities, F30 shows an overall higher velocity compared to the host rock. We observe these high velocities in the FWI velocity surfaces (Fig. 8c) and combined attribute (Fig. 8d). These observations are supported by our statistical analysis that shows F30 to generally have higher velocities along the fault (Fig. 8e, f) and across the fault (Fig. 8g). The fault zone velocity signature is much clearer in the case of F30 compared to F23, where the velocity difference between the fault zone and host rock is largely positive along-strike of the former (Fig. 8f).

Finally, Fault 26 (F26) is in the SW of the study area, away from the dome (Fig. 3c). F26 strikes ESE-WNW and is associated with several synthetic and antithetic faults in its hangingwall (Fig. 9a). F26 is clear in the PSDM variance surfaces, although a NNW-trending background fabric is also observed (Fig. 9b). This

fabric might be an acquisition footprint as it is aligned with the direction of the survey in-lines (see orientation of the blue dashed line in Fig. 1c). Unlike F23 and F30, F26 has different velocity expressions at the structural levels of H3 (i.e., low) and H7 (i.e., high) (Fig. 9c). The variable velocity with depth is also observed in the combined attribute, which defines F26 as a strong, laterally continuous red (positive) band at H7 level (Fig. 9d.2), whereas a generally blue, relatively less laterally continuous band is observed at the structural level of H3 (Fig. 8d.1). The dual behaviour of the fault zone is confirmed by our statistical analysis that shows F26 at the structural level of H3 is defined by velocities that are distinctively lower than surrounding host rock velocities (Fig. 9e.1, f.1). In contrast, at the structural level of H7, our statistical analysis confirms the overall higher velocity character shown by the other analysis, but also reveals more along-strike variability (Fig. 9e.2, f.2).

Discussion

We document changes in fault zone velocities that can be discerned both qualitatively (i.e., by visually examining velocity slices) and quantitatively (i.e., by extracting fault zone velocities and comparing them to surrounding velocities). Our results confirm that an FWI velocity model is capable of detecting fault zones (down to depth 1.5 km in our study area, limited only by a 6 km streamer length) as shown by the FWI variance that closely resembles the structures highlighted by the more traditional, PSDM variance slice (Figs. 3; 4). Along with detecting faults zones, the FWI velocity volume also captures variations in the physical properties of individual faults within the studied fault network and along-strike of individual faults. These differences in P-wave velocity within fault zones may be related to the presence of gases or fluids (i.e., gas clouds) potentially masking or amplifying velocity differences. Nonetheless, we argue that, when combined with other analyses (i.e., structural, stratigraphic analysis using seismic reflection datasets), FWI velocity models can reveal valuable information about the physical properties of fault zones. Mainly, we show that the FWI model shows differences in P-wave velocities among the studied fault network, which might be valuable not only to predicting fault's sealing potential (e.g., Welbon et al., 1997; Bailey et al., 2006), but also in capturing changes in fault zone architecture.

Across all scales, normal faults can have complex internal architecture, with variable fault core width, continuity (continuous along fault zone or discontinuous and patchy fault zones) and multiple slip surfaces (e.g., Michie & Haines, 2016). Previous studies show a range of factors can control fault zone architecture, including fault growth history (e.g., Childs et al., 2009), host rock lithology, pre-existing fabric, and the depth at which the fault is buried (e.g., see review by Wibberley et al., 2008). Laboratory experiments have also demonstrated the rheological differences in fault rocks can also result in variable

fault strength and stability (e.g., Bedford et al., 2022). The geometry and internal architecture of fault damage zones can also be controlled by slip mode at the fault's tips and the overall three-dimensional geometry of the fault plane (e.g., Kim et al., 2004). Regardless of the exact mechanism that determines fault zone architecture or extent of fault's damage zone, our current understanding of fault zone properties supports their variable and heterogeneous nature. We propose that the P-wave velocity anomalies we observe (Figs. 7-9) are likely a manifestation of the documented complexity of fault zone architecture and fault damage zones (e.g., Kim et al., 2004; Wibberley et al., 2008; Childs et al., 2009; Michie & Haines, 2016). Furthermore, the P-wave velocity anomalies might also reflect variability in fault seal condition within fault zones, which is something that needs to be considered in subsurface fluid flow models (i.e., during the characterisation of CCS sites or geothermal exploration targets, for example). Given the expected variation in P-wave velocities within faults zones, we investigate whether there are any overall correlations between high/low P-wave velocity anomalies with: i) regional present-day stress field and ii) conventional fault seal analysis results (SGR).

Previous studies in the Samson Dome have related fault opening and increased leakage to the present-day stress direction for faults offsetting shallow strata on the crest of the dome (e.g., Mattos et al., 2016). We hypothesise that faults that are likely leaking will show lower fault zone P-wave velocities. As leaking faults are often associated with increased permeability and/or fluid content, which lowers their P-wave velocities. By quantitively demonstrating the velocity differences between fault zones in the Samson Dome, we show that, overall, faults that strike NW-SE (i.e., parallel to the present-day maximum stress orientation; Heidbach et al., 2016) tend to have lower fault zone velocities (c. 3130 – 3140 m/s) compared to their surrounding host rock (c. 3180 – 3200 m/s; Fig. 7). In contrast, faults that strike E-W (i.e., perpendicular to the present-day maximum stress orientation) are characterised by higher fault zone velocities (up to c. 80 – 120 m/s higher fault zone velocities compared to host rock velocities; Fig. 8). However, our results also show that not all fault zone velocities of the studied fault network show a relationship to the present-day maximum stress orientation. For example, Fault 26 trends perpendicular to the present-day maximum stress orientation and instead of having higher fault zone velocities, shows variable fault zone velocities across different structural levels (Fig. 9). This variability might relate to the presence of interacting faults near the upper tip of the main fault.

Fault sealing potential and transmissibility are traditionally calculated using SGR (e.g., Manzocchi et al., 2010; Yielding et al., 2010). In this study, we explore the correlation between SGR and the observed P-wave velocity anomalies revealed by the FWI model. Alghuraybi et al. (2023) study the evolution of the

Samson Dome fault network and calculated SGR. They show that the studied fault network can be subdivided into two main subgroups: i) faults with vertical linkage and ii) faults that show no evidence of vertical linkage. The faults that show vertical linkage are generally associated with lower SGR (i.e., more likely to be leaking than sealing). These faults include F23, which we show here to have lower fault zone velocities across both H3 and H7 stratigraphic levels (Fig. 7). In contrast, F26 shows no evidence of vertical linkage and exhibits higher SGR values than F23 (Alghuraybi et al., 2023), which we show has higher fault zone velocities across the H7 stratigraphic level (Fig. 9.e2-g2). However, across the H3 stratigraphic level, F26 shows lower velocities than surrounding host rock (Fig. 9.e1-g1). The inconsistency between velocities across stratigraphic levels might hint at different factors controlling the studied fault zone properties, such as the natural heterogeneity in fault zones observed in outcrops (e.g., Kim et al., 2004; Wibberley et al., 2008; Childs et al., 2009; Michie & Haines, 2016). For instance, F26 has lower displacement at H3 compared to H7 (Alghuraybi et al., 2023). The lower displacement might result in thinner fault rock and narrower damage zone (e.g., Childs et al., 2009) at the H3 stratigraphic level compared to H7 for F26.

Even though interpretation workflows using seismic reflection data have significantly improved over the last decades (e.g., Jones & Knipe, 1996; Randen et al., 2001; Chopra & Marfurt, 2005; Fredman et al., 2008; Braathen et al., 2009; Iacopini & Butler, 2011; Iacopini et al., 2016), given the nature of the data used in these workflows, they are prone to be limited to only revealing fault geometries, fault facies and generally improve the imaging and visualisation of the fault networks. Our results demonstrate the potential of FWI models in recovering P-wave velocity within fault zones, which is something that cannot be achieved by using seismic reflection data alone. We suspect that the recovered P-wave velocities within fault zones are related to fault transmissibility. The variance attribute of the FWI model clearly highlights locations of rapid changes in P-wave velocity that coincides with the location and geometry of distortions in the PSDM volume, which we interpret as faults. However, not all of the faults we mapped in the PSDM volume are seen in the FWI model (Fig. 10. a, b). This may be related to the fact that some fault zones are too small to be resolved by FWI, or that some fault zones do not present as faster or slower velocity anomalies compared to the surrounding host rock. Outcrop data of fault zone thickness and displacement show a broad positive correlation between the two (e.g., Childs et al., 2009). Our results show that faults that have weak or no FWI signature tend to have average displacements of < 12 m, whereas those clearly visible on the FWI variance have an average displacement of c. 50 m (Fig. 10. c). We propose that by incorporating the information from the FWI velocity models, we can increase the fidelity of our subsurface interpretation by drawing from two separate datasets. Where two independent datasets converge, we can have more confidence in our subsurface interpretations and resulting models. The increased reliability

is something that is needed, especially in the field of subsurface geoscience to help the community meet energy transition policies and demands while providing essential public reassurance to the wider society about future implementations of carbon capture and geologic storage, geothermal energy, radioactive waste disposal sites, and mitigating seismic hazards. However, to fully test the hypothesis that FWI can serve as a screening tool for fault transmissibility, it is crucial to obtain pressure data from sites of fluid injection in the subsurface. This direct constraint on fault transmissibility would provide more conclusive evidence.

Conclusions

Our study demonstrates the effectiveness of Full-Waveform Inversion (FWI) velocity models in recovering the velocity structure of fault zones. By analysing the variance (i.e., edge attribute) of both the Post-Stack Depth Migrated (PSDM) seismic reflection volume and FWI model, we observe 'edges' with identical locations and geometries. These 'edges' correspond to locations of rapid changes in velocity and distortions in post-stack seismic traces, which we interpret as faults. However, not all faults visible in the PSDM are detectable in the FWI model. This discrepancy may be due to certain fault zones being too small to be resolved by FWI or not exhibiting significant velocity anomalies compared to the surrounding host rock. Many fault zones display variability in their P-wave velocity structure, reflecting the natural heterogeneity observed in faults from outcrop studies. In the FWI model, some faults (or parts of faults) appear as low-velocity anomalies, while others exhibit high velocities compared to the host rock. We hypothesise that this variability may be attributed to fault transmissibility. Furthermore, there is a partial correlation between fault velocity anomalies, the regional present-day stress field, and the results of Shale Gouge Ratio (SGR) analysis. However, it is important to acknowledge the presence of large uncertainties in the SGR analysis, which may limit its ability to provide a reliable indication of fault transmissibility in the Samson Dome. To fully test our hypothesis, we need more data (i.e., pressure and core data) from wellbores that are drilled across some of the faults where the FWI model exists to test predictions of fault transmissibility derived from FWI P-wave velocity models. Nonetheless, the results from our study are promising in terms of the effectiveness of FWI as a tool to predict physical properties of fault zones.

Acknowledgements

The results presented here are part of AA's PhD research at Imperial College London, funded by Saudi Aramco. We thank the Norwegian Petroleum Directorate for the publicly available data (https://portal.diskos.cgg.com/whereoil-data/) and Schlumberger for Petrel software. We would like to thank the Landscapes and Basins Research Group (LBRG) at Imperial College London, specifically Laura Frahm, for their valuable contributions and insightful discussions during the various stages of preparing this work.

Author contributions

AA: data analysis, investigation, conceptualisation, writing – original draft; RB: conceptualisation, supervision, writing – review & editing; CJ: conceptualisation, supervision, writing – review & editing

Funding

The results presented here are part of AA's PhD research at Imperial College London, funded by Saudi Aramco.

Data availability

The seismic and wellbore data are openly available in the Norwegian national data repository for petroleum data at https://portal.diskos.cgg.com/whereoil-data/.

References

Alghuraybi, A., Bell, R., Jackson, A-L., C. 2023. The Role of Normal Fault Growth History in Influencing Fault Seal Potential, Samson Dome, Offshore Norway [Preprint]. *EarthArXiv*, [last accessed 31 August 2023].

Alaei, B., & Torabi, A. 2017. Seismic imaging of fault damaged zone and its scaling relation with displacement. Interpretation, **5**(4), SP83-SP93. https://doi.org/10.1190/INT-2016-0230.1

An, Y., Guo, J., Ye, Q., Childs, C., Walsh, J., & Dong, R. 2021. Deep convolutional neural network for automatic fault recognition from 3D seismic datasets. *Computers & Geosciences*, ***153***, 104776. https://doi.org/10.1016/j.cageo.2021.104776

An, Y., Du, H., Ma, S., Niu, Y., Liu, D., Wang, J., Du, Y., Childs, C., Walsh, J., & Dong, R. 2023. Current state and future directions for deep learning based automatic seismic fault interpretation: A systematic review. *Earth-Science Reviews*, 104509. https://doi.org/10.1016/j.earscirev.2023.104509

Bedford, J. D., Faulkner, D. R., & Lapusta, N. 2022. Fault rock heterogeneity can produce fault weakness and reduce fault stability. *Nature communications*, ***13***(1), 326. https://doi.org/10.1038/s41467-022-27998-2

Botter, C., Cardozo, N., Hardy, S., Lecomte, I., Paton, G., & Escalona, A. 2016. Seismic characterisation of fault damage in 3D using mechanical and seismic modelling. Marine and Petroleum Geology, **77**, 973-990. https://doi.org/10.1016/j.marpetgeo.2016.08.002

Boyer, S. E., & Elliott, D. 1982. Thrust systems. *AAPG Bulletin*, ***66***(9), 1196-1230. https://doi.org/10.1306/03B5A77D-16D1-11D7-8645000102C1865D

Braathen, A., Tveranger, J., Fossen, H., Skar, T., Cardozo, N., Semshaug, S. E., ... & Sverdrup, E. 2009. Fault facies and its application to sandstone reservoirs. *AAPG bulletin*, ***93***(7), 891-917. https://doi.org/10.1306/03230908116

Braathen, A., Tveranger, J., Fossen, H., Skar, T., Cardozo, N., Semshaug, S. E., Bastesen, E., & Sverdrup, E. 2009. Fault facies and its application to sandstone reservoirs. *AAPG bulletin*, ***93***(7), 891-917. https://doi.org/10.1306/03230908116

Breivik, A. J., Gudlaugsson, S. T., & Faleide, J. I. 1994. Ottar Basin, SW Barents Sea: a major Upper Palaeozoic rift basin containing large volumes of deeply buried salt. Basin research, **7**(4), 299-312. https://doi.org/10.1111/j.1365-2117.1995.tb00119.x

Bretan, P. 2023. Assessing the predictive capability of the empirical Shale Gouge Ratio–buoyancy pressure calibration: implications for estimating CO2 column heights. *Geological Society, London, Special Publications*, ***528***(1), SP528-2022. https://doi.org/10.1144/SP528-2022-32

British Geological Survey (BGS). 2022. A scoping study for a deep geological carbon dioxide storage research facility. https://www.bgs.ac.uk/download/a-scoping-study-for-a-deep-geological-carbon-dioxide-storage-research-facility/

Chiaramonte, L., White, J. A., & Trainor-Guitton, W. 2015. Probabilistic geomechanical analysis of compartmentalization at the Snøhvit CO2 sequestration project. *Journal of Geophysical Research: Solid Earth*, ***120***(2), 1195-1209. https://doi.org/10.1002/2014JB011376

Childs, C., Manzocchi, T., Walsh, J. J., Bonson, C. G., Nicol, A., & Schöpfer, M. P. 2009. A geometric model of fault zone and fault rock thickness variations. *Journal of Structural Geology*, ***31***(2), 117-127. https://doi.org/10.1016/j.jsg.2008.08.009

Childs, C., Nicol, A., Walsh, J. J., & Watterson, J. 2003. The growth and propagation of synsedimentary faults. *Journal of Structural geology*, ***25***(4), 633-648. https://doi.org/10.1016/S0191-8141(02)00054-8

Chopra, S., & Marfurt, K. J. 2005. Seismic attributes—A historical perspective. *Geophysics*, ***70***(5), 3SO-28SO. https://doi.org/10.1190/1.2098670

Daniilidis, A., Nick, H. M., & Bruhn, D. F. 2021. Interference between geothermal doublets across a fault under subsurface uncertainty; implications for field development and regulation. *Geothermics*, **91**, 102041. https://doi.org/10.1016/j.geothermics.2021.102041

Davy, R. G., Frahm, L., Bell, R., Arai, R., Barker, D. H., Henrys, S., Bangs, N., Morgan, J., & Warner, M. 2021. Generating high-fidelity reflection images directly from full-waveform inversion: Hikurangi subduction zone case study. *Geophysical Research Letters*, ***48***(19), e2021GL094981. https://doi.org/10.1029/2021GL094981

de Laguna, W., Tamura, T., Weeren, H. O., Struxness, E. G., McClain, W. C., & Sexton, R. C. 1968. *Engineering development of hydraulic fracturing as a method for permanent disposal of radioactive wastes.* Oak Ridge National Lab. United States. https://doi.org/10.2172/4481039

Doré, A. G. 1995. Barents Sea geology, petroleum resources and commercial potential. *Arctic*, 207-221. https://doi.org/10.14430/arctic1243

Faleide, J. I., Tsikalas, F., Breivik, A. J., Mjelde, R., Ritzmann, O., Engen, Ø., Wilson, J., & Eldholm, O. 2008. Structure and evolution of the continental margin off Norway and the Barents Sea. Episodes, **31**(1), 82–91. https://doi.org/10.18814/epiiugs/2008/v31i1/012

Faleide, Jan I., Vågnes, E., & Gudlaugsson, S. T. 1993. Late Mesozoic-Cenozoic evolution of the south-western Barents Sea in a regional rift-shear tectonic setting. Marine and Petroleum Geology, **10**(3), 186–214. https://doi.org/10.1016/0264-8172(93)90104-Z

Faleide, Jan Inge, Gudlaugsson, S. T., & Jacquart, G. 1984. Evolution of the western Barents Sea. Marine and Petroleum Geology, **1**(2), 70–78. https://doi.org/10.1016/0264-8172(84)90082-5

Fredman, N., Tveranger, J., Cardozo, N., Braathen, A., Soleng, H., Røe, P., Skorstad, A., & Syversveen, A. R. 2008. Fault facies modeling: Technique and approach for 3-D conditioning and modeling of faulted grids. *AAPG bulletin*, ***92***(11), 1457-1478. https://doi.org/10.1306/06090807073

Freeman, B., Yielding, G., & Badley, M. 1990. Fault correlation during seismic interpretation. *First Break*, ***8***(3). https://doi.org/10.3997/1365-2397.1990006

Gabrielsen, R. H. 1984. Long-lived fault zones and their influence on the tectonic development of the southwestern Barents Sea. *Journal of the Geological Society*, ***141***(4), 651–662. https://doi.org/10.1144/gsjgs.141.4.0651

Gabrielsen, Roy H., Sokoutis, D., Willingshofer, E., & Faleide, J. I. 2016. Fault linkage across weak layers during extension: An experimental approach with reference to the Hoop Fault Complex of the SW Barents Sea. *Petroleum Geoscience*, ***22***(2), 123–135. https://doi.org/10.1144/petgeo2015-029

Gray, M., Bell, R. E., Morgan, J. V., Henrys, S., Barker, D. H., & IODP Expedition 372 and 375 Science Parties. 2019. Imaging the shallow subsurface structure of the North Hikurangi Subduction Zone, New Zealand, using 2-D full-waveform inversion. *Journal of Geophysical Research: Solid Earth*, ***124***(8), 9049-9074. https://doi.org/10.1029/2019JB017793

Heidbach, O., Rajabi, M., Reiter, K., Ziegler, M., & Wsm Team. 2016. World stress map database release 2016. *GFZ Data Services*, ***10***. doi:10.5880/WSM.2016.001

Hesthammer, J., Landrø, M., & Fossen, H. 2001. Use and abuse of seismic data in reservoir characterisation. *Marine and Petroleum Geology*, ***18***(5), 635-655. https://doi.org/10.1016/S0264-8172(01)00011-3

Iacopini, D., & Butler, R. W. 2011. Imaging deformation in submarine thrust belts using seismic attributes. *Earth and Planetary Science Letters*, ***302***(3-4), 414-422. https://doi.org/10.1016/j.epsl.2010.12.041

Iacopini, D., Butler, R. W. H., Purves, S., McArdle, N., & De Freslon, N. 2016. Exploring the seismic expression of fault zones in 3D seismic volumes. *Journal of Structural Geology*, ***89***, 54-73. https://doi.org/10.1016/j.jsg.2016.05.005

Jones, G., & Knipe, R. J. 1996. Seismic attribute maps; application to structural interpretation and fault seal analysis in the North Sea Basin. *First Break*, ***14***(12). https://doi.org/10.3997/1365-2397.1996024

Kaldi, J., Daniel, R., Tenthorey, E., Michael, K., Schacht, U., Nicol, A., Underschultz, J., & Backe, G. 2013. Containment of CO2 in CCS: Role of Caprocks and Faults. *Energy Procedia*, **37**, 5403-5410. https://doi.org/10.1016/j.egypro.2013.06.458

Kim, Y. S., Peacock, D. C., & Sanderson, D. J. 2004. Fault damage zones. *Journal of structural geology*, ***26***(3), 503-517. https://doi.org/10.1016/j.jsg.2003.08.002

Manzocchi, T., Childs, C., & Walsh, J. J. 2010. Faults and fault properties in hydrocarbon flow models. Geofluids, **10**(1-2), 94-113. https://doi.org/10.1111/j.1468-8123.2010.00283.x

Mattos, N. H., Alves, T. M., & Omosanya, K. O. 2016. Crestal fault geometries reveal late halokinesis and collapse of the Samson Dome, Northern Norway: Implications for petroleum systems in the Barents Sea. *Tectonophysics*, ***690***, 76–96. https://doi.org/10.1016/j.tecto.2016.04.043

Meldahl, P., Heggland, R., Bril, B., & de Groot, P. 2001. Identifying faults and gas chimneys using multiattributes and neural networks. *The leading edge*, ***20***(5), 474-482. https://doi.org/10.1190/1.1438976

Michie, E. A. H., & Haines, T. J. 2016. Variability and heterogeneity of the petrophysical properties of extensional carbonate fault rocks, Malta. Petroleum Geoscience, **22**(2), 136-152. https://doi.org/10.1144/petgeo2015-027

Morell, K. D., Regalla, C., Amos, C., Bennett, S., Leonard, L., Graham, A., Reedy, V., Levson, A., & Telka, A. 2018. Holocene surface rupture history of an active forearc fault redefines seismic hazard in southwestern British Columbia, Canada. *Geophysical Research Letters*, ***45***(21), 11-605. https://doi.org/10.1029/2018GL078711

Morgan, J., Warner, M., Bell, R., Ashley, J., Barnes, D., Little, R., Roele, K., & Jones, C. 2013. Next-generation seismic experiments: wide-angle, multi-azimuth, three-dimensional, full-waveform inversion. *Geophysical Journal International*, ***195***(3), 1657-1678. https://doi.org/10.1093/gji/ggt345

Morris, A. P., Ferrill, D. A., Sims, D. W., Franklin, N., & Waiting, D. J. 2004. Patterns of fault displacement and strain at Yucca Mountain, Nevada. *Journal of Structural Geology*, ***26***(9), 1707-1725. https://doi.org/10.1016/j.jsg.2003.12.005

NPD. 2023. Factpages Wellbore 7224/7-1. https://factpages.npd.no/en/wellbore/PageView/Exploration/All/1245

Randen, T., Pedersen, S. I., & Sønneland, L. 2001. Automatic extraction of fault surfaces from three-dimensional seismic data. *SEG Technical Program Expanded Abstracts*, ***20***(1), 551–554. https://doi.org/10.1190/1.1816675

Tromp, J. 2020. Seismic wavefield imaging of Earth's interior across scales. *Nature Reviews Earth & Environment*, ***1***(1), 40-53. https://doi.org/10.1038/s43017-019-0003-8

Virieux, J., & Operto, S. 2009. An overview of full-waveform inversion in exploration geophysics. *Geophysics*, ***74***(6), WCC1-WCC26.

Warner, M., Ratcliffe, A., Nangoo, T., Morgan, J., Umpleby, A., Shah, N., Vinje, V., Štekl, I., Guasch, L., Win, C., Conroy, G., & Bertrand, A. 2013. Anisotropic 3D full-waveform inversion. *Geophysics*, **78**(2), R59-R80. https://doi.org/10.1190/geo2012-0338.1

Wernicke, B. 1995. Low-angle normal faults and seismicity: A review. *Journal of Geophysical Research: Solid Earth*, ***100***(B10), 20159-20174. https://doi.org/10.1029/95JB01911

Wibberley, C. A., Yielding, G., & Di Toro, G. 2008. Recent advances in the understanding of fault zone internal structure: a review. *Geological Society, London, Special Publications*, ***299***(1), 5-33. https://doi.org/10.1144/SP299.2

Wrona, T., Pan, I., Bell, R. E., Gawthorpe, R. L., Fossen, H., & Brune, S. 2021. 3D seismic interpretation with deep learning: A brief introduction. *The Leading Edge*, ***40***(7), 524-532. https://doi.org/10.1190/tle40070524.1

Yielding, G. P. B. S., Bretan, P., & Freeman, B. 2010. Fault seal calibration: a brief review. *Geological Society, London, Special Publications*, **347**(1), 243-255. https://doi.org/10.1144/SP347.14

Figure captions

Figure 1. (a) Stratigraphic column summarising the seismic stratigraphic framework and horizon names and ages as constrained by wellbore 7224/7-1. **(b)** Location map for the study area. **(c)** Depth map at the H3 level highlighting the outline of the Samson Dome and some of the faulting in the area. The location of wellbore 7224/7-1 is denoted by a blue star and the blue and red dash lines outline the location of the depth and FWI sections shown in Fig. 2.

Figure 2. Representative in-line **(a)** and cross-line **(b)** with FWI data (top) and seismic reflection depth data (bottom). The sections show the faulted nature of the area that can be seen in both FWI and depth sections. Also, these sections highlight the lateral velocity changes across faults especially in **(b)**. The dashed circle shows a case where a fault is offsetting two blocks of different velocities while the dashed rectangle highlights faults with apparent detectable fault zone velocities that are different than adjacent strata.

Figure 3. (a) FWI velocity data extracted along the L. Cretaceous H3 surfaces showing a general decrease in velocity towards the centre (towards the dome) but also highlights velocity variations along and across faults. **(b)** FWI variance attribute revealing some of the faults. The geometry of the fault network can be seen clearly by the variance surface extracted along the H3 level **(c)**.

Figure 4. (a) FWI velocity data extracted along the L. Jurassic H7 surfaces showing a general decrease in velocity towards the centre (towards the dome) but also highlights velocity variations along and across faults. **(b)** FWI variance attribute revealing some of the faults. The geometry of the fault network can be seen clearly by the variance surface extracted along the H7 level **(c)**.

Figure 5. A cartoon illustration of the fault zone velocity extraction methodology used in this study.

Figure 6. A summary of the workflow used in this study to map and analyse the fault network and FWI velocity variations.

Figure 7. (a) a cross-section view of fault 23 using FWI (a.1) and PSDM (a.2) data. **(b)** A variance slice showing the lateral extent and geometry of fault 23 along H3 (b.1) and H7 (b.2) levels. The

yellow dashed line in (b.1) shows the location of the cross sections in (a) and velocity profile in (g). **(c)** FWI slices showing the velocity differences between the fault zone and surrounding area. **(d)** Velocity detection attribute showing lower fault zone velocity on both H3 (d.1) and H7 (d.2) levels. The results from **(d)** are compared with quantitative analysis of the fault zone velocity along the fault **(e & f)** and across the fault **(g)**. Fault zone velocities are shown in blue while host rock velocities are shown in grey colour in **(e). (f)** shows the difference between the two velocity categories. The location of the fault zone is shown by the shaded yellow colour in **(g)** and the length of the profile is denoted by L**.**

Figure 8. (a) a cross-section view of fault 30 using FWI (a.1) and PSDM (a.2) data. **(b)** A variance slice showing the lateral extent and geometry of fault 30 along H3 (b.1) and H7 (b.2) levels. The yellow dashed line in (b.1) shows the location of the cross sections in (a) and velocity profile in (g). **(c)** FWI slices showing the velocity differences between the fault zone and surrounding area. **(d)** Velocity detection attribute showing higher fault zone velocity on both H3 (d.1) and H7 (d.2) levels. The results from **(d)** are compared with quantitative analysis of the fault zone velocity along the fault **(e & f)** and across the fault **(g)**. Fault zone velocities are shown in blue while host rock velocities are shown in grey colour in **(e). (f)** shows the difference between the two velocity categories. The location of the fault zone is shown by the shaded yellow colour in **(g)** and the length of the profile is denoted by L**.**

Figure 9. (a) a cross-section view of fault 26 using FWI (a.1) and PSDM (a.2) data. **(b)** A variance slice showing the lateral extent and geometry of fault 26 along H3 (b.1) and H7 (b.2) levels. The yellow dashed line in (b.1) shows the location of the cross sections in (a) and velocity profile in (g). **(c)** FWI slices showing the velocity differences between the fault zone and surrounding area. **(d)** Velocity detection attribute showing lower fault zone velocity on H3 (d.1) and higher velocity on H7 (d.2) levels. The results from **(d)** are compared with quantitative analysis of the fault zone velocity along the fault **(e & f)** and across the fault **(g)**. Fault zone velocities are shown in blue while host rock velocities are shown in grey colour in **(e). (f)** shows the difference between the two velocity categories. The location of the fault zone is shown by the shaded yellow colour in **(g)** and the length of the profile is denoted by L**.**

Figure 10. (a) FWI variance attribute extracted along the H7 level. **(b)** The spatial distribution of the studied fault network colour-coded by response strength on the FWI variance attribute. Fault names are labelled on the map in (b). **(c)** Box plots showing the displacement distribution of the faults grouped by strength of FWI variance signature.

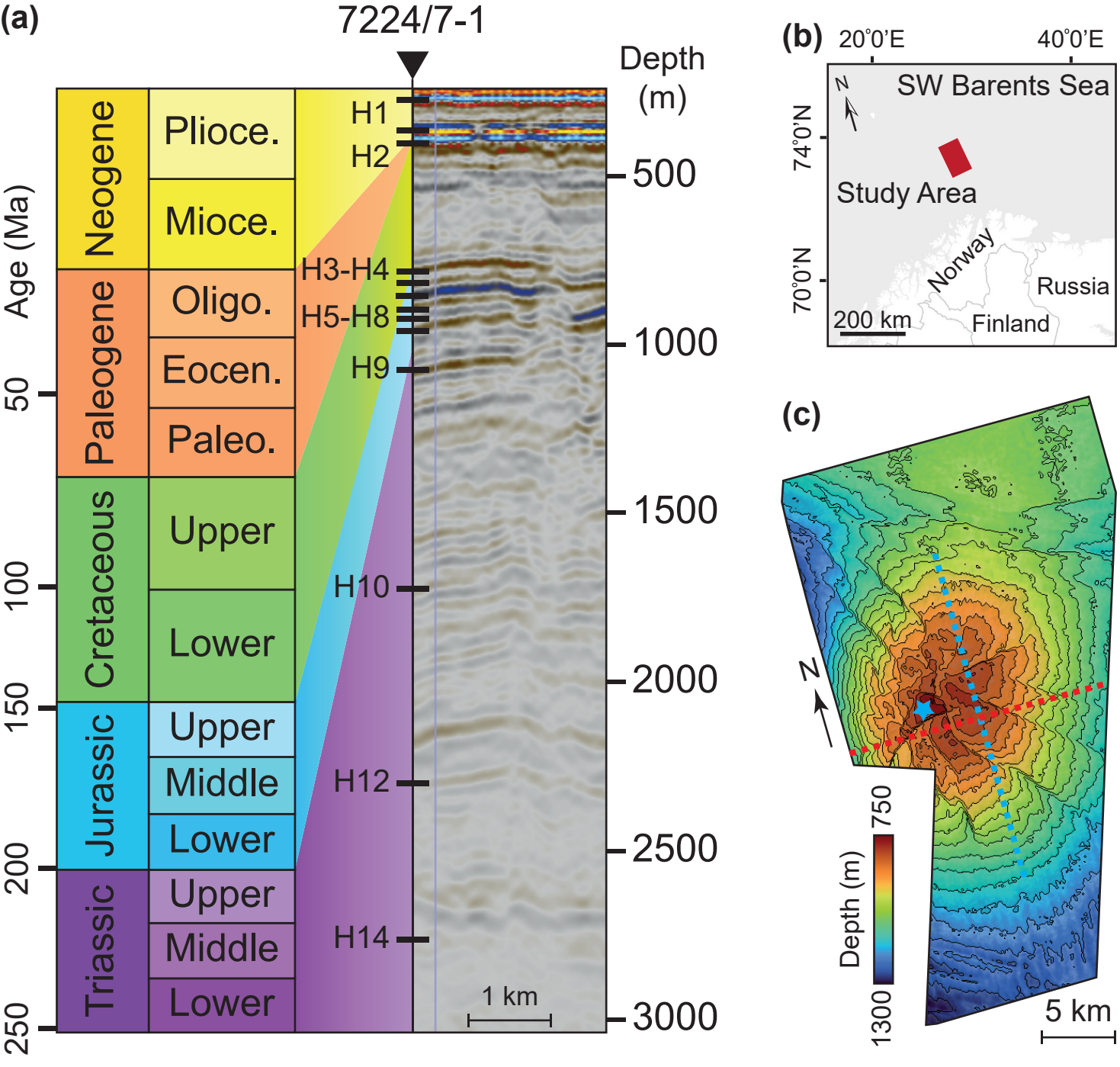

Figure 1. (a) Stratigraphic column summarising the seismic stratigraphic framework and horizon names and ages as constrained by wellbore 7224/7-1. (b) Location map for the study area. (c) Depth map at the H3 level highlighting the outline of the Samson Dome and some of the faulting in the area. The location of wellbore 7224/7-1 is denoted by a blue star and the blue and red dash lines outline the location of the depth and FWI sections shown in Fig. 2.

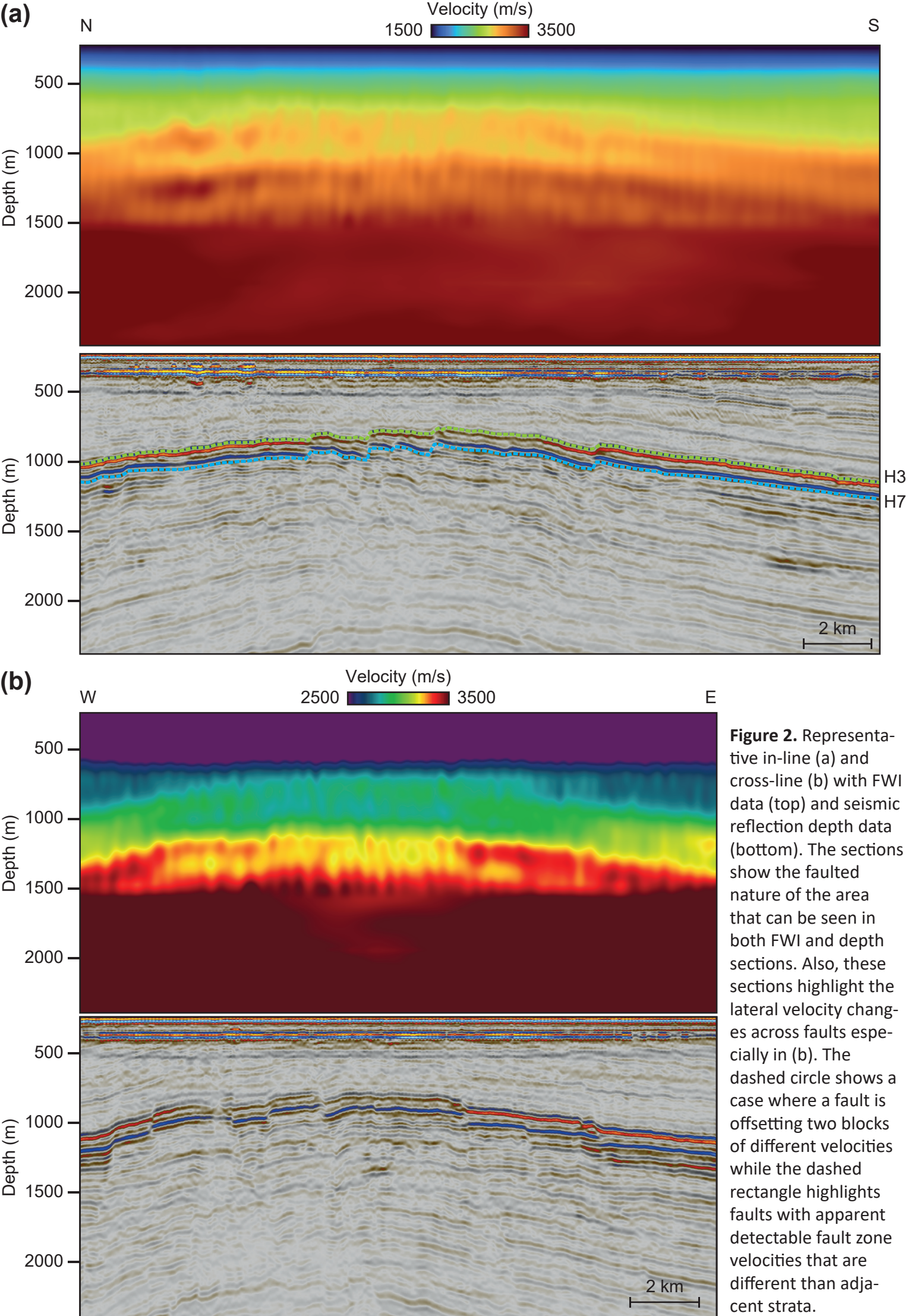

Figure 2. Representative in-line (a) and cross-line (b) with FWI data (top) and seismic reflection depth data (bottom). The sections show the faulted nature of the area that can be seen in both FWI and depth sections. Also, these sections highlight the lateral velocity changes across faults especially in (b). The dashed circle shows a case where a fault is offsetting two blocks of different velocities while the dashed rectangle highlights faults with apparent detectable fault zone velocities that are different than adjacent strata.

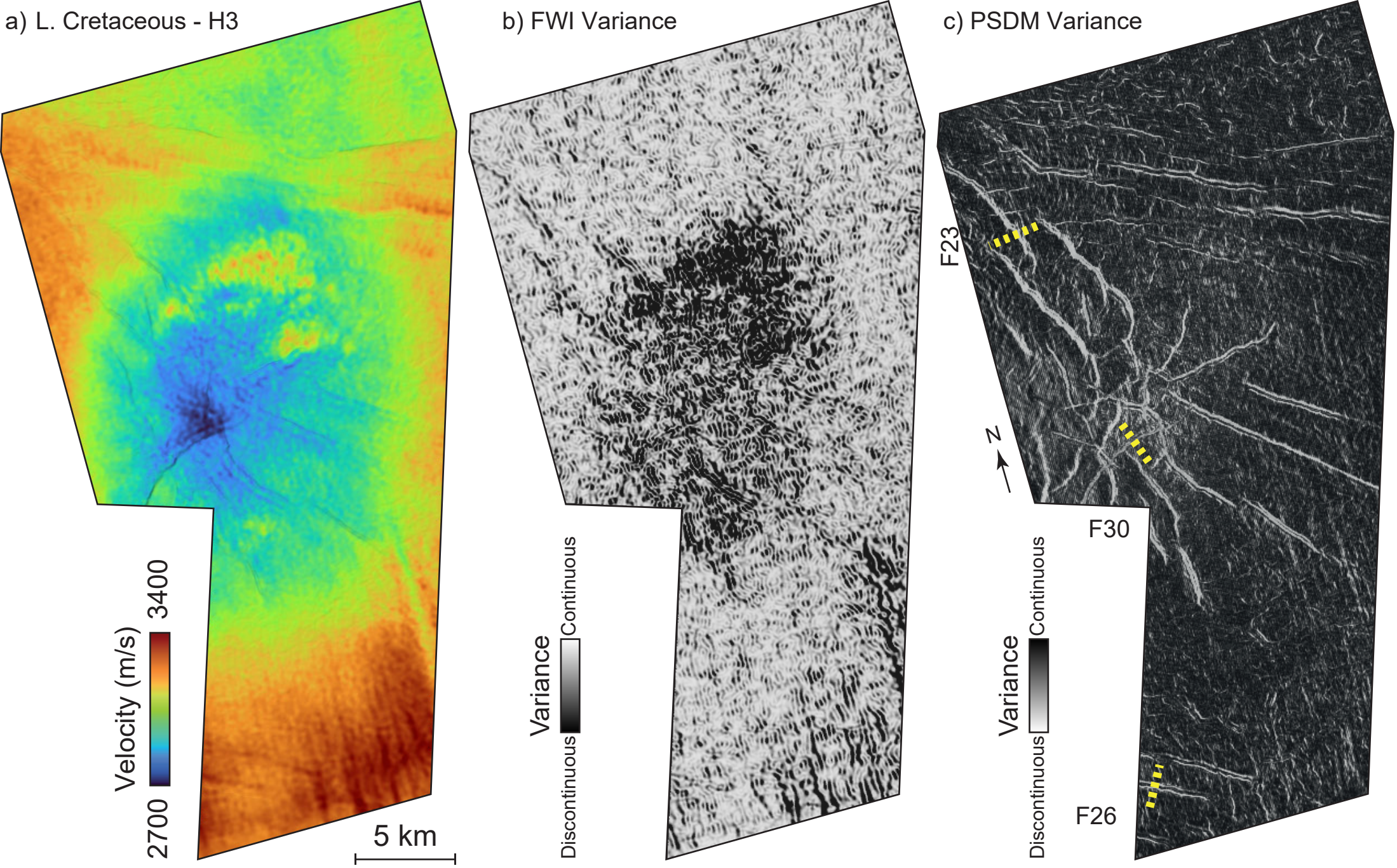

Figure 3. (a) FWI velocity data extracted along the L. Cretaceous H3 surfaces showing a general decrease in velocity towards the centre (towards the dome) but also highlights velocity variations along and across faults. (b) FWI variance attribute revealing some of the faults. The geometry of the fault network can be seen clearly by the variance surface extracted along the H3 level (c).

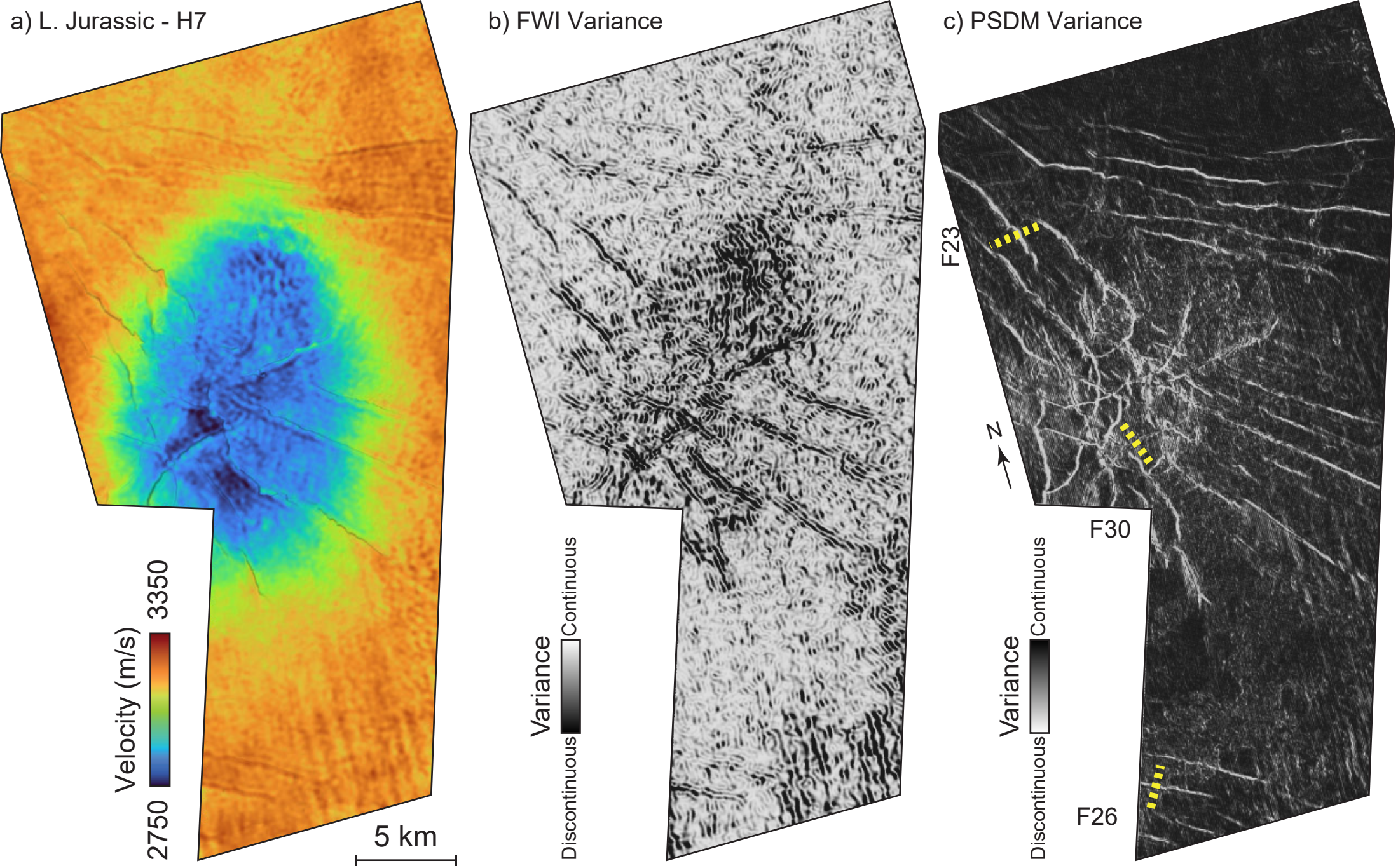

Figure 4. (a) FWI velocity data extracted along the L. Jurassic H7 surfaces showing a general decrease in velocity towards the centre (towards the dome) but also highlights velocity variations along and across faults. (b) FWI variance attribute revealing some of the faults. The geometry of the fault network can be seen clearly by the variance surface extracted along the H7 level (c).

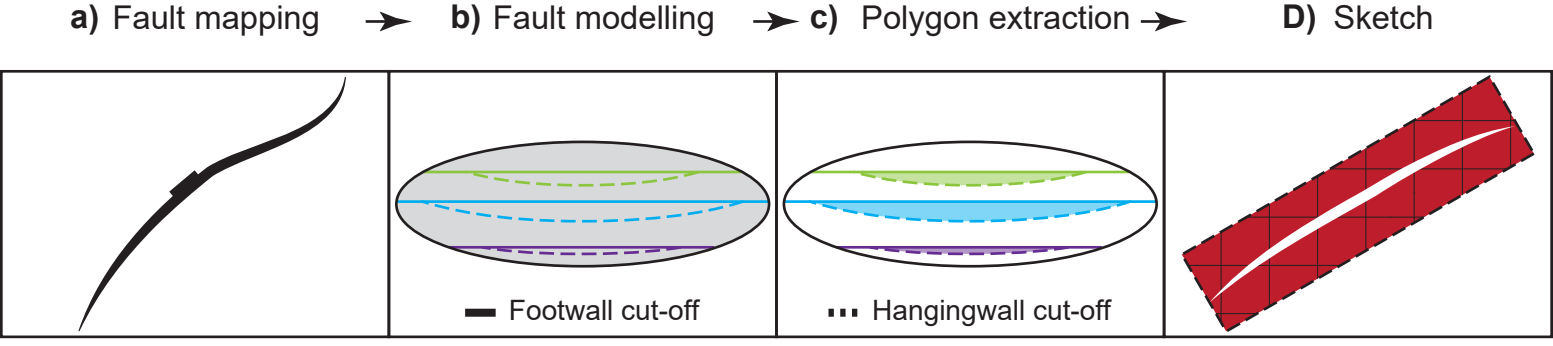

Figure 5. A cartoon illustration of the fault zone velocity extraction methodology used in this study.

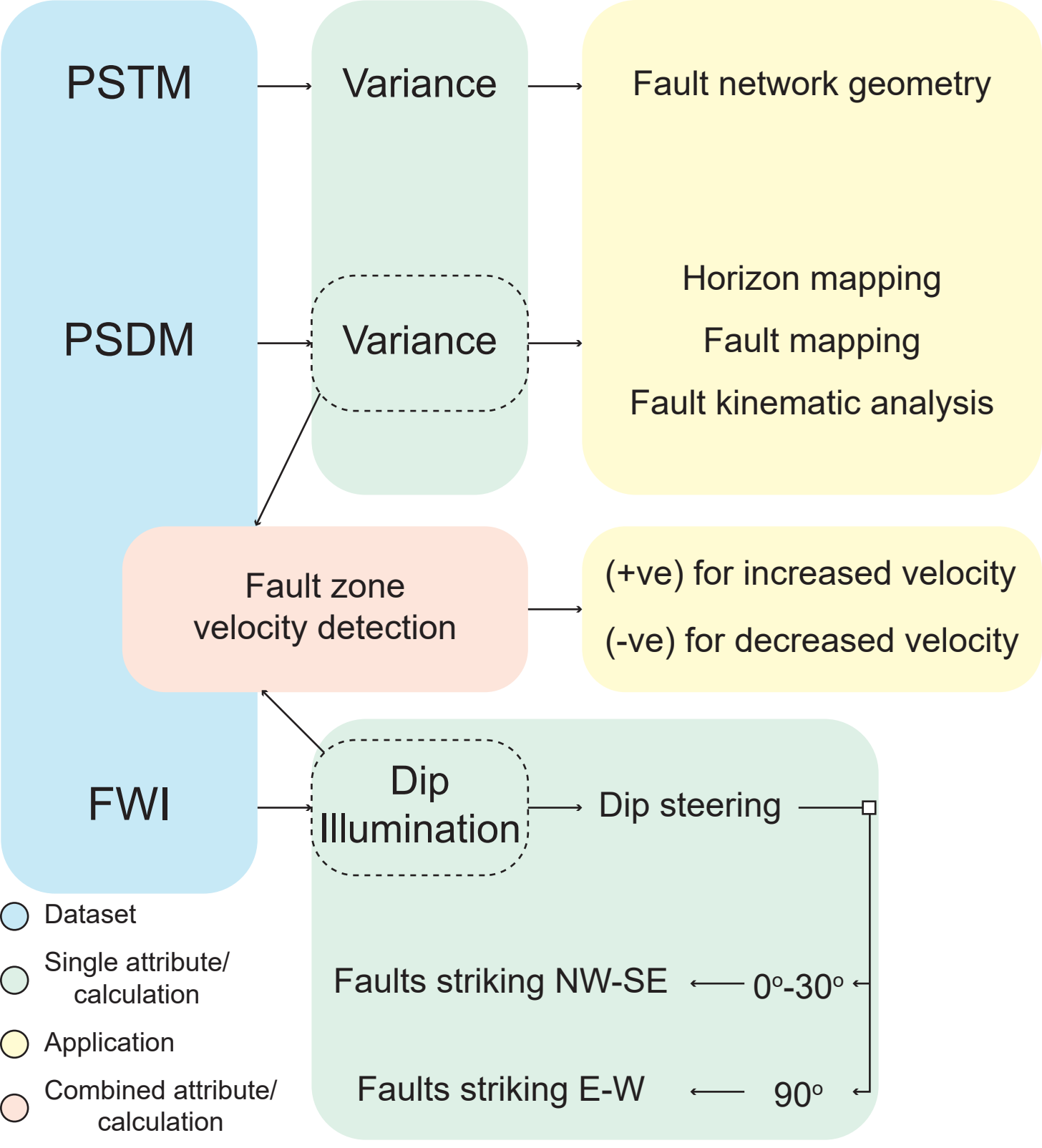

Figure 6. A summary of the workflow used in this study to map and analyse the fault network and FWI velocity variations.

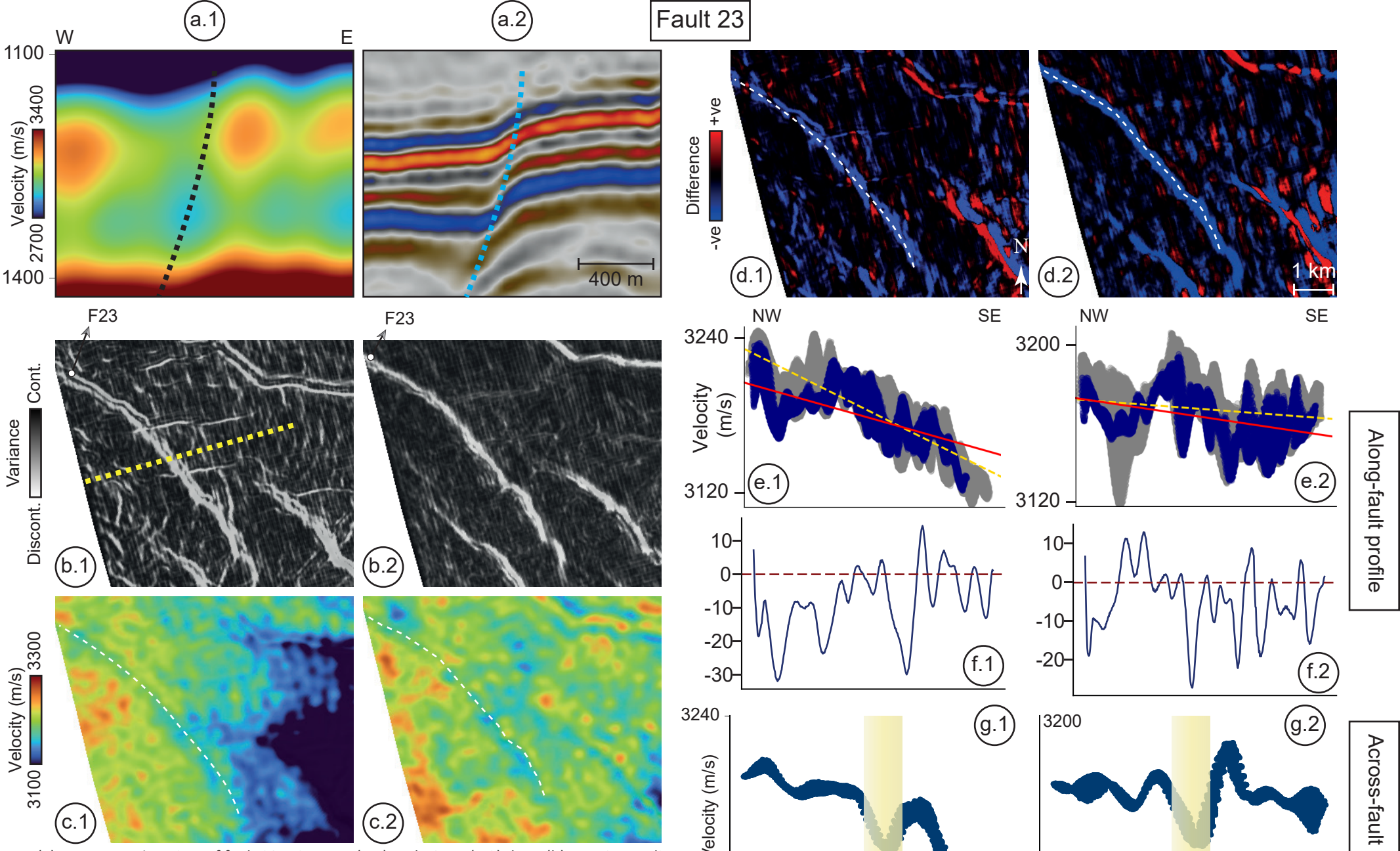

Figure 7. (a) a cross-section view of fault 23 using FWI (a.1) and PSDM (a.2) data. (b) A variance slice showing the lateral extent and geometry of fault 23 along H3 (b.1) and H7 (b.2) levels. The yellow dashed line in (b.1) shows the location of the cross sections in (a) and velocity profile in (g). (c) FWI slices showing the velocity differences between the fault zone and surrounding area. (d) Velocity detection attribute showing lower fault zone velocity on both H3 (d.1) and H7 (d.2) levels. The results from (d) are compared with quantitative analysis of the fault zone velocity along the fault (e & f) and across the fault (g). Fault zone velocities are shown in blue while host rock velocities are shown in grey colour in (e). (f) shows the difference between the two velocity categories. The location of the fault zone is shown by the shaded yellow colour in (g) and the length of the profile is denoted by L.

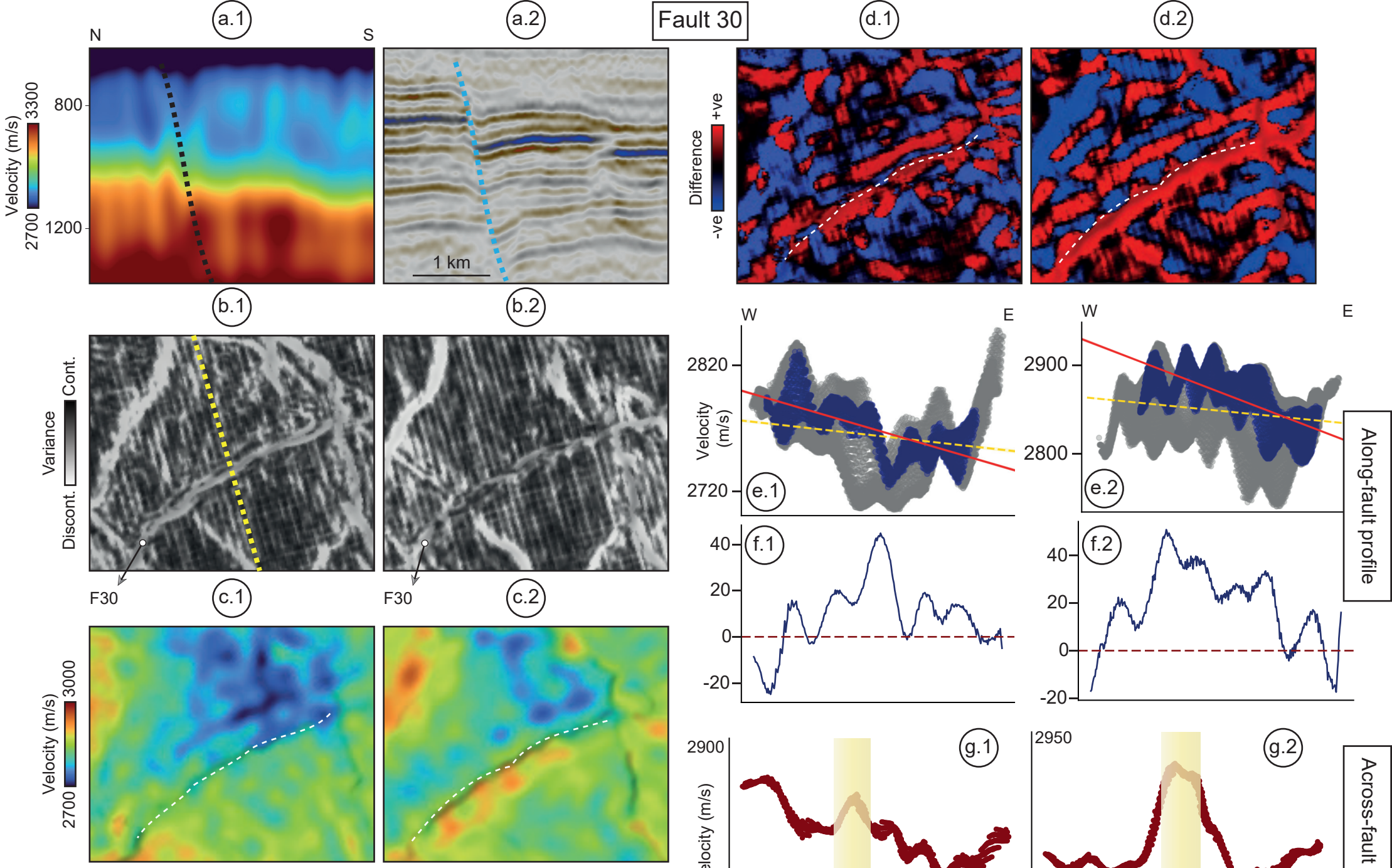

Figure 8. (a) a cross-section view of fault 30 using FWI (a.1) and PSDM (a.2) data. (b) A variance slice showing the lateral extent and geometry of fault 30 along H3 (b.1) and H7 (b.2) levels. The yellow dashed line in (b.1) shows the location of the cross sections in (a) and velocity profile in (g). (c) FWI slices showing the velocity differences between the fault zone and surrounding area. (d) Velocity detection attribute showing higher fault zone velocity on both H3 (d.1) and H7 (d.2) levels. The results from (d) are compared with quantitative analysis of the fault zone velocity along the fault (e & f) and across the fault (g). Fault zone velocities are shown in blue while host rock velocities are shown in grey colour in (e). (f) shows the difference between the two velocity categories. The location of the fault zone is shown by the shaded yellow colour in (g) and the length of the profile is denoted by L.

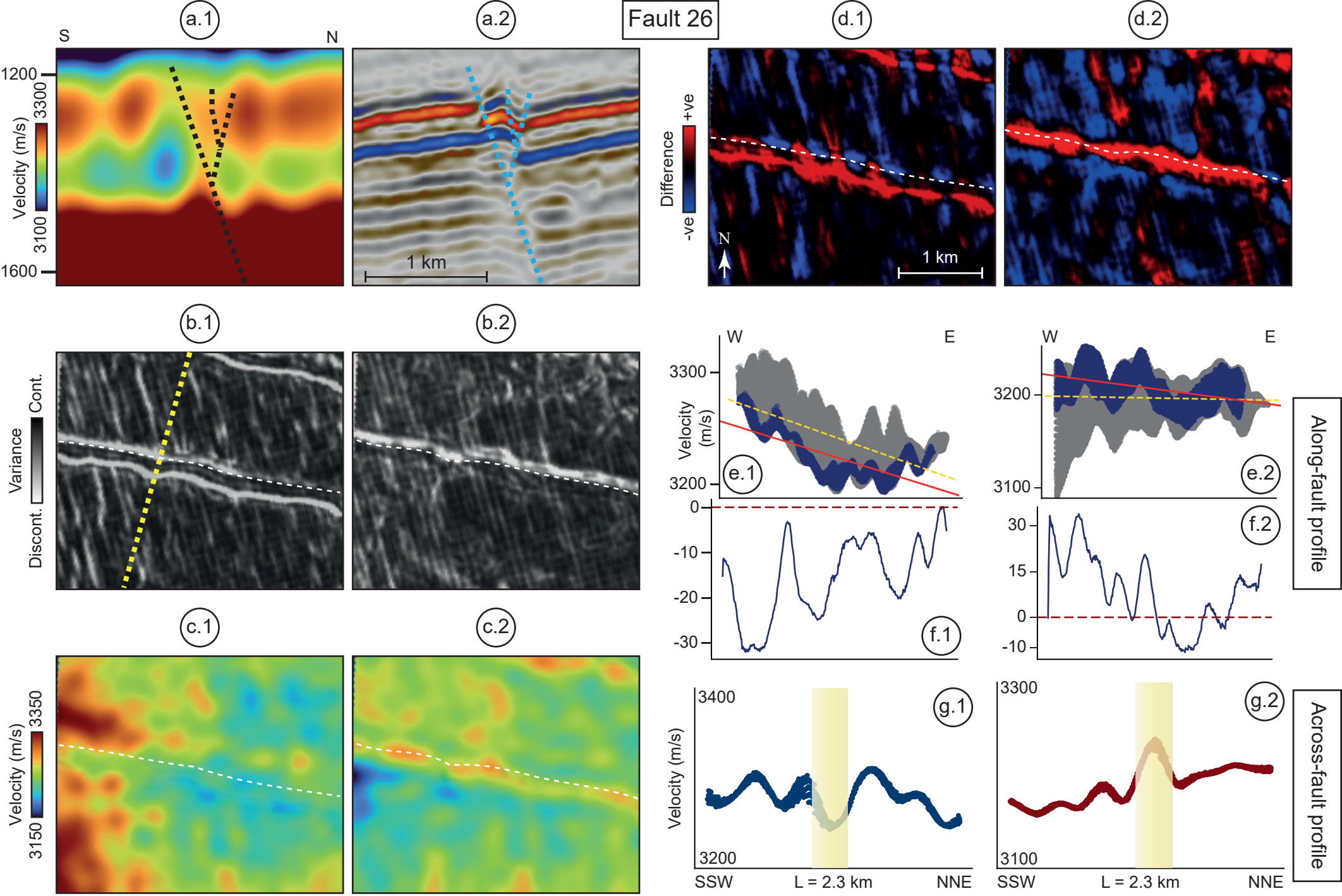

Figure 9. (a) a cross-section view of fault 26 using FWI (a.1) and PSDM (a.2) data. (b) A variance slice showing the lateral extent and geometry of fault 26 along H3 (b.1) and H7 (b.2) levels. The yellow dashed line in (b.1) shows the location of the cross sections in (a) and velocity profile in (g). (c) FWI slices showing the velocity differences between the fault zone and surrounding area. (d) Velocity detection attribute showing lower fault zone velocity on H3 (d.1) and higher velocity on H7 (d.2) levels. The results from (d) are compared with quantitative analysis of the fault zone velocity along the fault (e & f) and across the fault (g). Fault zone velocities are shown in blue while host rock velocities are shown in grey colour in (e). (f) shows the difference between the two velocity categories. The location of the fault zone is shown by the shaded yellow colour in (g) and the length of the profile is denoted by L.

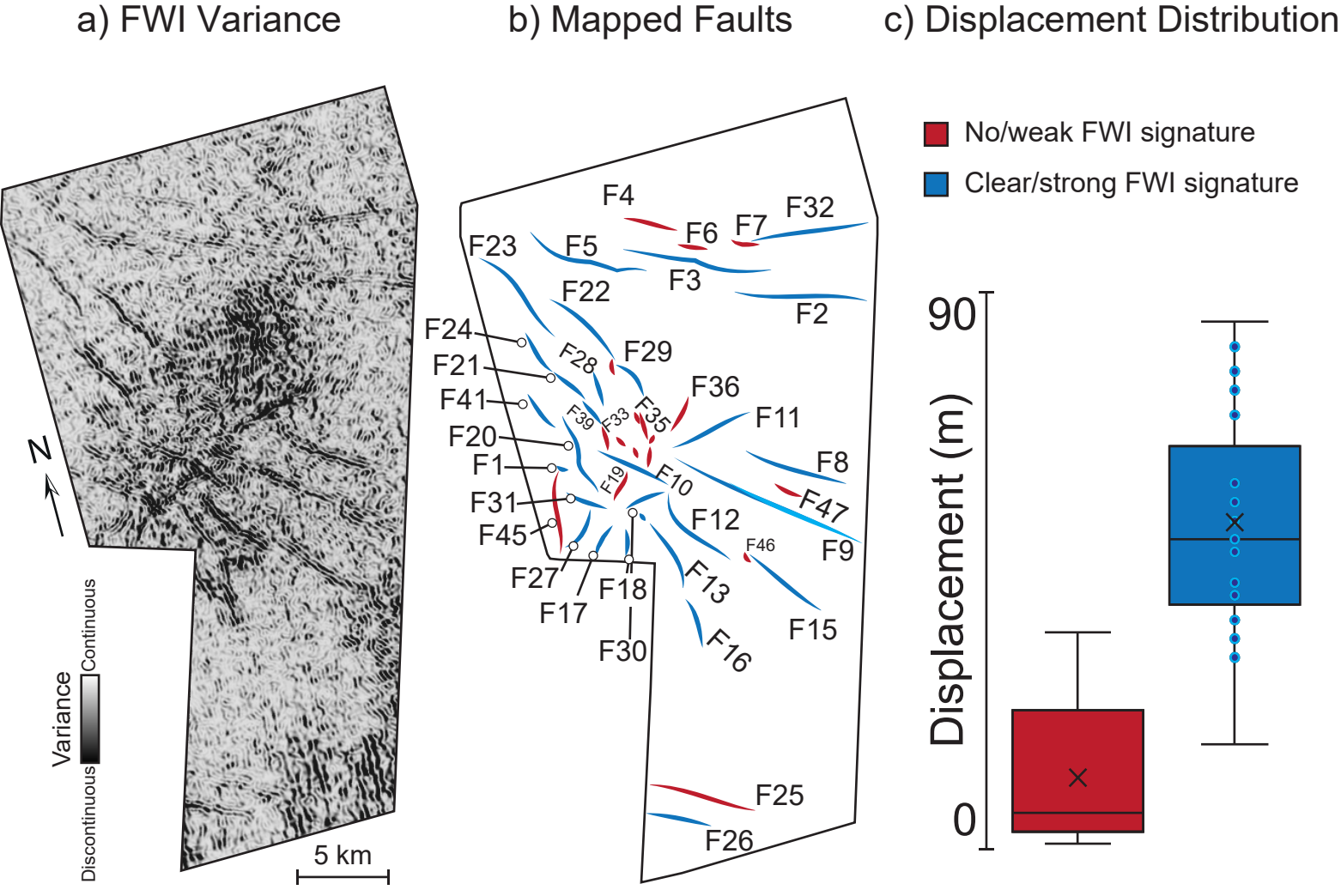

Figure 10. (a) FWI variance attribute extracted along the H7 level. (b) The spatial distribution of the studied fault network colour-coded by response strength on the FWI variance attribute. Fault names are labelled on the map in (b). (c) Box plots showing the displacement distribution of the faults grouped by strength of FWI variance signature.

Appendix 1. Depth slices at 400 m, 800 m, 1200 m and 1600 m across the PSDM and FWI volumes and their associated variance attributes. These depth slices showcase the dramatic decrease in the FWI resolution after 1.5 km.